



Numerical and experimental investigation of added resistance of different ship types in short and long waves

Sebastian Sigmund, Ould el Moctar

Show more

Outline Share Cite

<https://doi.org/10.1016/j.oceaneng.2017.10.010>

[Get rights and content](#)

Highlights

- Advanced computational methods and procedures for reliable prediction of added resistance in short and long waves.
- Assessment of added resistance in waves based on Computational Fluid Dynamics and physical tests for different ship types.
- Effects of viscosity on added resistance in short and long waves.
- Effects of wave steepness on added resistance in short and long waves.
- Effects of ship speed on the added resistance in short and long waves.

Abstract

Added resistance in short and long regular head waves for four different ship types was systematically and extensively investigated using Reynold-averaged Navier Stokes solvers. Computations, which included ship motions and added resistance, were validated against scale model test measurements. Effects of ship speed, skin friction, wave steepness, ship type, as well as wave radiation and wave diffraction on added resistance were analyzed.

Previous

Next

Keywords

Added resistance in waves; Ship motions; Computational fluid dynamics; Physical tests; Wave steepness; Added friction resistance in waves; Ship types

1. Introduction

The installed power of a ship is usually defined by the contractual agreed design speed. The design speed needs to be proven by the shipyard during sea trials. The environmental conditions, contractually specified for these sea trials, usually represent nearly ideal fair weather conditions: the prevailing wind speed does not exceed two on the Beaufort scale, and the significant wave height of the seaway is stipulated at less than 0.5 m. The disadvantage of this approach is that a ship is optimized for conditions it may hardly ever experience, and the so-called sea margin is generally considered to be independent of ship size or type. This may lead to both underpowered smaller and overpowered larger ships operating in the same sea areas, due to size-dependent ship responses. Increasing operational costs and business competition led ship operators to critically scrutinize the fuel consumption of their fleet and, consequently, ships are requested to be designed and optimized for operational conditions. Therefore, it stands to reason to challenge and possibly adapt current design procedures to optimize ships for near-service operational conditions. Thus, prediction of the added resistance of ships in waves is of high practical interest. Naturally, therefore, a considerable amount of research effort has been devoted to this problem. The techniques used to predict added resistance can be classified in two main categories, namely, far-field methods, based on considering the diffracted and radiated wave energy and momentum flux at infinity, and near-field methods, based on direct integration of the steady second-order hydrodynamic pressure acting on the wetted ship surface. Maruo (1957) introduced the first far-field approach, which was later extended by Maruo, 1960, Maruo, 1963 and Joosen (1966). Boese (1970) developed the first near-field direct pressure integration method, albeit by considering a highly simplified pressure distribution. Gerritsma and Beukelman (1972) introduced the radiated energy approach, which basically followed Maruo's far-field approach. Evaluating the above approaches, Ström-Tejse et al., 1973 found large discrepancies between the numerical results and comparative model test measurements. Using ship motions obtained from the strip theory of Salvesen et al., 1970, Salvesen, 1978 obtained satisfactory predictions by applying Gerritsma and Beukelman's method, thereby confirming the importance of accurate ship motion predictions to reliably estimate added resistance in waves. By introducing a simplified added resistance formula to model the complicated interaction of diffracted waves and the steady flow around the ship, Faltinsen et al. (1980) presented a more accurate potential theory near-field direct pressure integration approach. In this way, they validated their results even for short waves. Recently, Liu et al. (2011) used a well-established frequency domain panel method and a new hybrid time domain Rankine source Green function method to predict the added resistance in waves by obtaining first-order velocity potentials and Kochin functions, terms necessary to compute added resistance according to Maruo's far-field method. They used a wide range of case studies to validate their results and concluded that their method is satisfactory to predict added resistance of ships in waves. The recently developed three-dimensional Rankine panel method accounts for the interaction of the linear periodic wave-induced flow with the nonlinear steady flow caused by the ship's forward speed in calm water, taking into account nonlinear free surface conditions and dynamic squat (Söding et al., 2012). In this method, added resistance in waves is obtained by pressure integration. Kashiwagi et al. (2010) also investigated the prediction accuracy of added resistance in short waves when forward speed is present and attributed inaccuracies to hydrodynamic nonlinear effects.

Added resistance in waves was investigated by many researchers using potential theory, Kim and Kim, 2011, Kim et al., 2012, Lyu and el Moctar, 2017, Duan and Li, 2013, Guo and Steen, 2011, Kuroda et al., 2008, Seo et al., 2013, Seo et al., 2014, Sportelli and Huijsmans, 2012, Turnock et al., 2014 and Söding et al. (2014). While boundary element methods based on Rankine sources are efficient and, therefore, predominantly used to screen relevant wave scenarios for design issues, Computational Fluid Dynamics (CFD) methods based on the numerical solution of Reynolds-averaged Navier-Stokes (RANS) or Euler equations are increasingly applied to account for nonlinearities, braking waves, etc. They demonstrated their ability to provide results of comparable accuracy to model test measurements in many problems of ship hydrodynamics (Larsson et al., 2010, Oberhagemann et al., 2012, el Moctar, 2001, el Moctar et al., 2011, el Moctar et al., 2016a, Schellin and el Moctar, 2007, Carrica et al., 2011). However, their applications to added resistance predictions are still rare. Although such methods might, in principle, directly address also the problem of power increase in irregular waves, both long waves (and the correspondingly large ship motions) and short waves (which contribute to the added resistance through diffraction) should be resolved simultaneously, which increases significantly the required grid size and computational time. Therefore, the application of CFD methods to the added resistance problem has been limited so far mainly to regular wave situations in a restricted range of wave frequencies (el Moctar et al., 2016b, Ley et al., 2014, Sadat-Hosseini et al., 2013, Simonsen et al., 2013).

The present investigation employed RANS-based field methods to systematically investigate added resistance in short and long regular head waves for four selected ship types, namely, a medium-size cruise ship, a post-Panamax containership, a tanker, and a Wigley hull. Computations, which included ship motions, were validated against scale model test measurements. Particular emphasis was placed on the following research questions:

- How accurate and reliable are Reynolds-averaged Navier Stokes (RANS) solvers to predict wave added resistance, and how are the results influenced by discretization errors?

- How does ship speed influence the added resistance in waves?
- How does friction affect the added resistance in waves?
- How does the radiation and diffraction problem interact in a nonlinear regime? Can they be considered separately?
- How do wave height and wave steepness affect the added resistance in waves, and does the assumption of the quadratic dependence on wave amplitude also hold in steep waves?

2. Numerical method

We document only a brief overview of the [numerical methods](#) used. A detailed description can be found in [Ferziger and Peric \(2002\)](#) and [Muzafferija and Peric \(1999\)](#).

The in-house modified interDymFoam ([OpenFOAM, 2011–2016](#)) and the *COMET* ([CD ADAPCO, 2011](#)) Reynolds-averaged Navier-Stokes (RANS) solvers were employed to compute the flow surrounding the subject ships in calm water and in waves. Both solvers use the [Finite Volume Method](#) (FVM) to solve the conservation equations. The solution domain is divided into Control Volumes (CV) for which the RANS equations are solved in integral form. For an incompressible, isothermal, and [viscous fluid](#) of density ρ , the conservation equations of mass and momentum in integral form read as follows:

$$\frac{d}{dt} \int_V \rho dV + \int_S \rho (\vec{v} - \vec{v}_s) \cdot \vec{n} dS = 0 \quad (1)$$

$$\frac{d}{dt} \int_V \rho \vec{v} dV + \int_S \rho \vec{v} (\vec{v} - \vec{v}_s) \cdot \vec{n} dS = \int_V \vec{T} \cdot \vec{n} dS + \int_V \vec{b} dV \quad (2)$$

In the momentum Equation (2), the surface and volume forces are included in the [stress tensor](#), \vec{T} , and in the body forces, \vec{b} , respectively, where V is the control volume, \vec{v} is the fluid velocity, and \vec{v}_s is the velocity of the control volume's surface, s . The stress tensor includes [viscous shear stress](#) and a pressure term, p , multiplied by the unit tensor, \vec{I} :

$$\vec{T} = \mu \left\{ \nabla \vec{v} + \nabla \vec{v}^T \right\} - p \vec{I} \quad (3)$$

where μ is the [dynamic viscosity](#). A second order scheme discretizes time derivatives using constant time steps, specifically, the Implicit Three Time Level in *COMET* and the Crank-Nicholson method in OpenFOAM ([Ferziger and Peric, 2002](#)).

To obtain a dedicated pressure equation, the mass equation is converted into a Poisson equation used for pressure correction of the [velocity field](#). The Semi-Implicit Method for Pressure-Linked Equations (SIMPLE) algorithm implemented in *COMET* provides an implicit coupling between pressure and velocity ([Ferziger and Peric, 2002](#)). At each time step, [outer iterations](#) correct pressures and velocities iteratively. Software OpenFOAM employs the PIMPLE algorithm (Combination PISO/SIMPLE) ([OpenFOAM, 2016](#)).

To simulate a floating body at a free water surface, a [two-phase flow](#) needs to be modeled. The solvers use the interface capturing Volume-Of-Fluid (VOF) technique, which has proven to be suitable for handling complex free surface phenomena ([Muzafferija and Peric, 1999](#)). It introduces an additional transport equation to compute the spatial distribution of scalar [volume fraction](#) α in the fluid domain. Fraction α describes the fluid properties, specifically, effective density and viscosity in each control volume. The effective fluid density, ρ_{eff} , is defined as follows:

$$\rho_{eff} = \alpha \rho_{water} + (1 - \alpha) \rho_{air} \quad (4)$$

where ρ_{water} and ρ_{air} are the densities of water and air, respectively. Viscosity is computed in the same manner. To guaranty a sharp free water surface, *COMET* employs the High-Resolution Interface-Capturing (HRIC) scheme to discretize α transport equation ([Muzafferija and Peric, 1999](#)). In OpenFOAM the Multidimensional Universal [Limiter](#) with Explicit Solution (MULES)-algorithm is used to compute the spatial distribution of the volume fraction.

At inlet boundaries, a transient wave boundary condition prescribes velocity and surface elevation according to linear wave theory. In the fluid [domain](#), [velocity](#), pressure, and α fields are initialized. Nonlinear ship motions are computed by an implicit six Degree of Freedom (DOF) solver coupled implicitly with RANS equations ([Brunswig and el Moutar, 2004](#), [el Moutar et al., 2017](#)). Accordingly, a mesh morphing algorithm deforms the numerical grid to move ships in the computational domain ([Oberhagemann and el Moutar, 2007](#)). The two equation $k-\epsilon$ and $k-\omega-SSP$ [turbulence models](#) are used to close the system of equations ([Menter, 1994](#)). For the [turbulent boundary layer](#), shear stresses on the hull are determined using logarithmic wall functions.

3. Selected test cases

To cover a wide range of practical needs, we investigated the phenomenon of wave added resistance for a wide range of conventional ship types as well as for a well known test case, [Fig. 1](#). Specifically, our studies were performed for a modern medium-size cruise ship ([Ley et al., 2014](#), [Valanto and Hong, 2015](#)), a post-Panamax 14000 TEU containership referred to as the Duisburg Test Case (DTC) ([el Moutar et al., 2010](#), [el Moutar et al., 2016b](#), [Sprengrer et al., 2016](#)), the medium-size MOERI tanker KVLCC2 ([Simman, 2008](#)), and the well-known Wigley hull ([Journée, 2003](#)). [Fig. 1](#) shows their hull shapes. Beside the ship length, the [block coefficient](#) varied significantly, as it may have a significant influence on wave added resistance.

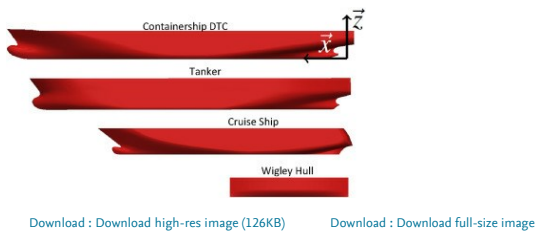


Fig. 1. Hull forms of the investigated ships.

Extensive model tests in calm water and in waves were performed for all test cases. The Hamburg Ship Model Basin HSVA ([Valanto and Hong, 2015](#)) performed model test for the cruise ship; the Norwegian Marine Technology Research Institute MARINTEK ([Sprengrer et al., 2016](#)) and the SVA Potsdam ([Nietzschmann, 2010](#)), for the containership; the Maritime & Ocean Engineering Research Institute (MOERI), for the tanker; and the Technical University Delft, for the Wigley Hull. [Table 1](#) summarizes main particulars of the four ships and [Table 2](#) the associated tests conditions.

Table 1. Main particulars of the investigated ships (full scale).

	Symbols	Cruise Ship	Containership	Tanker	Wigley Hull
Length bet. perp. [m]	L	220.27	355.0	320.0	100.0
Breadth at waterline [m]	B	32.2	51.0	58.0	10.0
Scantling draft [m]	d	7.20	14.5	20.8	6.26
Displaced volume [m ³]	Δ	33229	173467	312622	2888
Wetted surface [m ²]	S_w	7822.8	22032.0	27194.0	1490.8
Block coefficient [-]	c_b	0.65	0.66	0.81	0.46
Froude number [-]	F_r	0.16, 0.22	0.05, 0.14	0.14	0.30
Model scale [-]	λ	1:36.0	1:63.65	1:100	1:33
Metacentric height [m]	GM	2.75	1.5	5.71	0.65
Vert. center of grav. [m]	VOG	15.05	19.86	18.60	5.61
Inertia radius [m ⁴]	I_{yy}	59.58	88.77	80.0	25.0
Non-dimensional wave length [-]	λ_w / L	0.22–1.09	0.2–2.0	0.22–2.5	0.5–2.0
Wave steepness [%]	λ_w / λ_w	2.5	1.0–8.0	1.4–8.0	0.6–2

Table 2. Test conditions in calm water and in waves (full scale).

Ship type	ρ_s [-]	λ_H/L [-]	λ_H [m]	λ_H/λ_H [%]
Cruiser Ship	0.16, 0.22	Calm Water		
		0.28	1.55	2.52
		0.39	2.17	2.53
		0.49	3.6	3.34
		0.66	3.6	2.48
		0.79	3.6	2.07
		0.89	3.6	1.84
		0.98	3.6	1.67
		1.09	3.6	1.50
		1.23	3.6	1.33
		1.41	3.6	1.16
		1.8	3.6	0.91
		2.5	3.6	0.65
Containership	0.14, 0.05	Calm Water		
		0.22	2.99	3.83
		0.28	5.66	5.70
		0.36	8.27	6.47
		0.44	12.09	7.74
		0.60	7.51	3.53
		0.80	9.93	3.50
		0.91	9.04	2.80
		1.00	10.18	2.87
		1.09	11.20	2.90
		1.20	10.18	2.39
		1.40	12.73	2.56
		1.80	12.73	1.99
		2.50	12.73	1.43
Tanker	0.14	Calm Water		
		0.2	6.0	4.69
		0.3	6.0	3.13
		0.4	6.0	2.34
		0.5	6.0	1.88
		0.6	6.0	1.56
		0.7	6.0	1.34
		0.9	6.0	1.04
		1.0	6.0	0.94
		1.1	6.0	0.85
		1.2	6.0	0.78
		1.4	6.0	0.67
		1.6	6.0	0.59
		1.8	6.0	0.52
Wigley Hull	0.30	Calm Water		
		0.50	1.35	2.71
		0.59	1.26	2.13
		0.75	1.37	1.82
		0.91	1.04	1.15
		1.00	1.19	1.19
		1.05	1.04	0.99
		1.11	0.91	0.82
		1.25	1.01	0.81
		1.38	0.90	0.65
		1.50	0.81	0.54
		1.75	1.42	0.81
		2.00	1.28	0.64

The physical models of the cruise ship and the containership were moored with soft springs in a diamond shaped or rectangular frame, respectively, which was towed at constant speed. These setups, schematically shown in Fig. 2, held the models captive and allowed them to move in surge, heave, and pitch. Transducers attached to the springs measured towing forces. The tanker KVLCC2 and the Wigley hull were free to heave and pitch. All other degrees of freedom were suppressed.

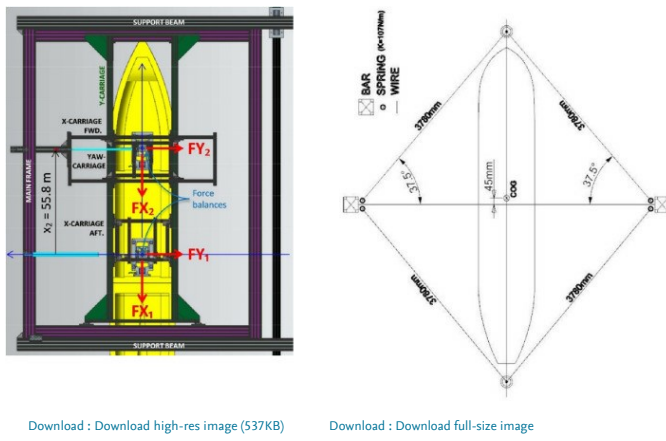


Fig. 2. Model test setups of mooring arrangement for the cruise ship (left) and the containership (right) (Valanto and Hong, 2015, Sprenger et al., 2016).

4. Computational procedure

Determining the wave added resistance, R_{aw} , of a ship comprises three steps. First, the calm water resistance, R_T , for each specific ship speed is computed. Second, the averaged longitudinal force in waves, F_X , is determined. The ships were free to heave and pitch. All other degrees of freedom were suppressed. Third, the wave added resistance is calculated by subtracting the calm water resistance from the time-averaged longitudinal force in waves. These steps, always performed in the same way, determine the frictional part of added resistance. For this procedure, it is essential to use the same numerical grids and test setups for all computations (in calm water as well as in waves) to minimize possible errors caused by spatial and temporal discretization, model test scale effects, and iterative computational techniques. The typical sample time history of computed longitudinal force presented in Fig. 3 was performed for model scale conditions on a numerical grid consisting of $3.2 \cdot 10^6$ control volumes, and it relied on a time step of 0.005s, whereby the Courant number, on average, was less than 0.5. In this Fig., the oscillating solid line identifies the total longitudinal force; the dashed line, the calm water longitudinal force; and the dash/dotted line, the time-averaged longitudinal force. The difference between dashed and dash/dotted line is equal to the added resistance in waves. Here, the tested ship was the Wigley Hull advancing at constant forward speed corresponding to a Froude number of $F_n = 0.3$ in regular 0.06 m high head waves corresponding to a wave length ratio of $\lambda_W/L = 1.9$, where λ_W is wave length and L is ship length between perpendiculars.

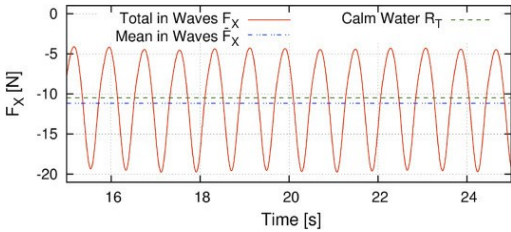


Fig. 3. Computed added resistance for the Wigley Hull (model scale) at $F_n = 0.30$ in regular head waves of $\lambda_W/L = 1.0$, $h_W = 0.06m$ obtained by subtracting calm water resistance (dashed line) from time-averaged longitudinal force in waves (dash/dotted line).

The time-averaged longitudinal force in waves as well as the ship motion amplitudes were obtained by performing a Fourier analysis of the time histories for selected time windows containing multiple encounter periods, see Fig. 11 below.

Computed and measured values of resistance amplitudes were normalized as follows:

$$C_{AW} = \frac{17(\bar{F}_X - R_T) L}{\rho g \zeta^2 \zeta_\theta} \quad (5)$$

$$C_R = \frac{R_T}{\rho \zeta} \quad (6)$$

$$C_Z = \frac{F_Z}{\rho \zeta} \quad (7)$$

here, C_{AW} is wave added resistance coefficient, \bar{F}_X the time averaged longitudinal force in waves, g is acceleration of gravity, B is ship breadth, ζ is wave amplitude, ζ_θ and θ_θ are heave and pitch amplitude, respectively, and $k = 2\pi/\lambda_W$ is wave number. For normalization it is essential to use actual computed (instead of target) wave amplitudes rather than target values. Therefore, amplitudes of undisturbed waves next to a ship's bow were monitored in all simulations.

The calm water resistance coefficient, c_T , reads as follows:

$$c_T = \frac{R_T}{0.5 \rho v^2 S_W} \quad (8)$$

where R_T is calm water resistance, ρ is water density, v is ship speed, and S_W is wetted hull surface.

As model tests are not suited to predict the frictional resistance component for ships, it is common practice to rely on the ITTC '57 guidelines (Hadler, 1958, International Towing Tank Conference, 2008) to specify a ships frictional resistance coefficient as follows:

$$c_F = \frac{0.075}{(\log Re)^2} \quad (9)$$

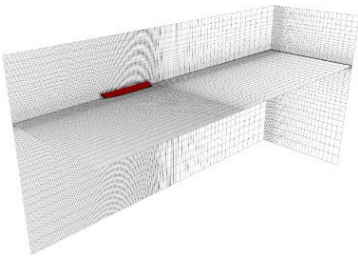
with the Reynolds number, $Re = vL/\nu$ being kinematic viscosity of water and L ship length between perpendiculars. Frictional resistance, R_F , then reads as follows:

$$R_F = C_F 0.5 \rho v^2 S_W \quad (10)$$

Response amplitude operators are plotted against the dimensionless wave frequency, ω , defined as follows:

$$\omega = \sqrt{L/g} \quad (11)$$

Computations were performed on unstructured grids consisting of hexahedral control volumes. Dimensions of the computational domain were orientated to the length of the ship models. The inlet boundary was located at least one model length ahead of the models' forward perpendicular to reduce the free running length of incident waves; the outlet boundary, at least three model lengths behind the models' aft perpendicular to avoid wave reflection; the side boundaries, two-and a-half model lengths to port and starboard of the models' central symmetry plane; the bottom, at two model lengths below the calm water surface; and the top, at one model length above the calm water surface. To illustrate, Fig. 4 shows the computational fluid domain for the cruise ship. To accurately resolve the wave pattern and the incident wave field, grids were locally refined in the vicinity of the free surface and in areas surrounding the hull. To dampen incident and hull-induced waves, the control volumes were smoothly stretched towards the outlet boundaries. To properly account for the boundary layer on the hull surface, prism layers were included and wall functions applied. The grids used comprised between $1.6 \cdot 10^6$ and $30.0 \cdot 10^6$ control volumes for the entire flow domain.



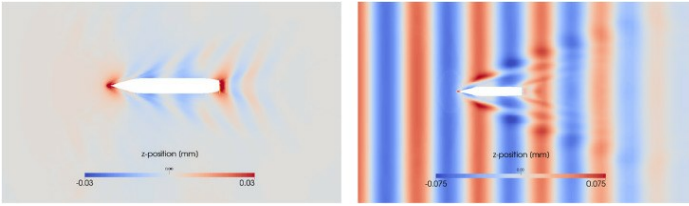
Download : [Download high-res image \(489KB\)](#)

Download : [Download full-size image](#)

Fig. 4. Sample of a typical numerical grid, here for the cruise ship.

At inlet [boundaries](#), [velocities](#), [volume fractions](#), [turbulent kinetic energies](#), and [dissipation](#) rates were specified. The hull surface was defined as no-slip walls. At outlet and top boundaries, hydrostatic boundary conditions were specified. The origin of the [inertial frames](#) was located on the ships' base line at their aft perpendiculars. The origin of the ship-fixed reference frames was situated at the ships' [center of gravity](#).

[Fig. 5](#) shows wave patterns in calm water (left) and in incoming waves (right) for the containership computed on the same numerical grid. Obviously, the ship induced wave pattern is more pronounced in waves. Furthermore, waves were damped behind the model to avoid wave reflection.

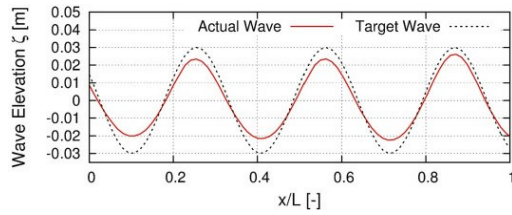


Download : [Download high-res image \(287KB\)](#)

Download : [Download full-size image](#)

Fig. 5. Computed wave pattern in calm water (left) and in regular head waves (right) of the containership at $Re = 0.2$, $\lambda_W/L = 1.125$, $h_W = 0.12m$

To reduce uncertainties related to [discretization errors](#), all computations were performed on the same grid using the same numerical setup. In short waves, numerical damping made it impossible to attain the specified wave amplitude; however, in waves longer than 0.6 times ship length ($\lambda_W/L > 0.6$), deviations between target and actual wave amplitude were nearly zero percent. Therefore, actually computed wave amplitudes of undisturbed waves next to a ship's bow were monitored in all simulations, and these amplitudes were used for normalization rather than as target values. [Fig. 6](#) exemplarily depicts target and actual wave amplitudes for the wave length $\lambda_W/L = 0.3$. For the tanker in wave lengths up to $\lambda_W/L = 0.6$, [Table 3](#) lists the percentage deviations of actual wave amplitudes from their target values. Deviations in longer waves were negligibly small.



Download : [Download high-res image \(265KB\)](#)

Download : [Download full-size image](#)

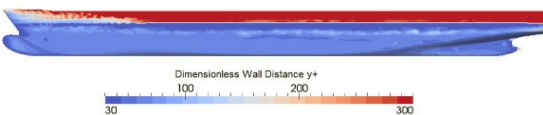
Fig. 6. Actual and target [short](#) wave amplitude near bow: KVLCC2, $Re = 0.142$, $\lambda_W/L = 0.3$

Table 3. Actual and target wave amplitude of short waves computations with the tanker.

λ_W/L [-]	Target Wave amp. [m]	Actual Wave amp. [m]	Deviation [%]
0.2	0.03	0.023	23
0.3	0.03	0.025	16.6
0.4	0.03	0.028	6.6
0.5	0.03	0.029	3.3
0.6	0.03	0.03	0

5. Discretization errors

To investigate the influence of spatial and temporal [discretization](#) on wave added resistance, grid studies for all ships were performed advancing in calm water as well as in waves. Hereto, grids were refined systematically by multiplying the grids' base size in all directions by a factor of about $\sqrt{1.7}$. Then, for each ship a coarse, a medium, and a fine grid comprising $1.6 \cdot 10^6$ to $7.5 \cdot 10^6$ control volumes, extending over both port and [starboard sides](#), were generated. For the containership, additional computations were conducted on a very fine grid comprising $20 \cdot 10^6$ control volumes. To minimize the influence of turbulence modeling and wall functions, the non-dimensional wall distance, y^+ , on hulls' wetted surfaces was kept constant for all grids at a mean value of approximately 80. [Fig. 7](#) depicts this situation for the containership at $Re = 0.20$.



Download : [Download high-res image \(168KB\)](#)

Download : [Download full-size image](#)

Fig. 7. Dimensionless wall distance, y^+ , on wetted surfaces of the containership at $Re = 1.0 \cdot 10^6$, $Re = 0.20$

For the containership and the cruise ship, Fig. 8 plots computed total and frictional calm water resistance coefficients, C_T and C_F , versus the total numbers of control volumes. Frictional resistance coefficients remain nearly constant, whereas total resistance coefficients decrease with increasing number of control volumes. The reason for this is numerical diffusion, which influenced the viscous pressure resistance and decreased on finer grids.

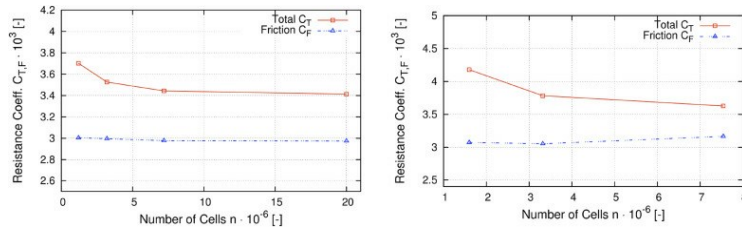


Fig. 8. Computed total and frictional calm water resistance coefficients versus number of control volumes for the containership (left) at $Fr = 0.20$ and $Re = 1.0 \cdot 10^7$ and the cruise ship (right) at $Fr = 0.16$ and $Re = 1.1 \cdot 10^7$, Sigmund and el Mocrat (2017).

Fig. 9 plots the computed wave added resistance coefficients, C_{AW} , obtained on different sized grids versus wave length to ship length ratio, λ_w/L , as well as normalized wave frequency, $(L/\lambda_w)^{1/2}$. The coarse grid comprised about $1.6 \cdot 10^6$ control volumes; the medium grid, about $3.2 \cdot 10^6$ control volumes; the fine grid, about $7.5 \cdot 10^6$ control volumes. Depending on a grid's spatial discretization, waves were damped, especially the short waves. To account for this damping, we performed computations using the computed (instead of the target) wave height. The relatively small deviations between coefficients computed on different sized grids led us to conclude that the spatial discretization did not significantly influence the normalized added resistance coefficient as long as the actual computed wave height was used for normalization. Part of this study was recently published by Sigmund and el Mocrat (2017).

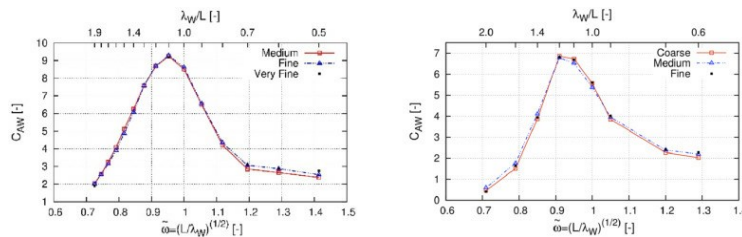


Fig. 9. Added resistance coefficient of the containership (left) at $Fr = 0.20$ and the tanker (right) at $Fr = 0.14$ versus normalized wave frequency and wave length to ship length ratio computed on different sized grids.

6. Results

All computations were performed at model scale on the medium sized numerical grid, which comprised about 3.2 million control volumes. The time step in computations corresponded to an average Courant number of 0.5. Table 4 summarizes the resulting calm water resistance, expressed in its normalized form as coefficient, C_T , obtained from computations and experimental measurements for the four ship types advancing at constant forward speeds. This table also lists the associated Froude number, Fr , as well as the percentage deviation between computed and measured values. These deviations are less than five percent, i.e., they are small and therefore deemed sufficiently accurate to carry on with our computations of the wave added resistance.

Table 4. Computed and measured calm water resistance coefficients.

Ship type	Fr [-]	$C_T \cdot 10^3$ [-]		Deviation [%]
		Computation	Experiment	
Cruise Ship	0.16	4.2	4.069	-3.22
	0.22	4.208	4.088	-2.95
Containership	0.05	4.487	4.623	3.02
	0.14	3.77	3.79	-0.45
Tanker	0.14	5.181	5.066	-2.264
Wigley Hull	0.30	1.449	1.384	-4.714

Fig. 10 presents time histories of computed and experimentally measured heave and pitch motions for the containership in regular head waves. The solid line identifies computed motions; the dotted line, experimentally measured motions. These motions are nearly harmonic and, generally, their amplitudes and phase angles compare favorably to measurements. The deviation between computed and measured amplitudes is less than 2%. Although not shown here, the corresponding time histories for the other three ships were similar; however, in the shortest waves, measured motions for these other ship types were not always harmonic.

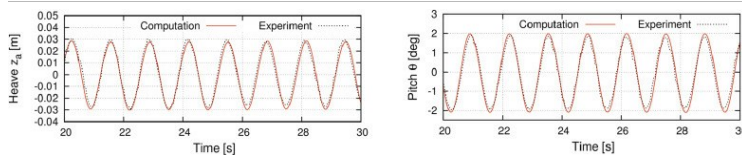


Fig. 10. Computed and measured time histories of heave (left) and pitch (right) motions of the containership at $Fr = 0.14$, $\lambda_w/L = 0.91$, $h_w = 0.14m$.

Fig. 11, Fig. 12, Fig. 13 presents time histories and mean values of computed longitudinal force, F_x , for the four investigated ships advancing at constant forward speed in calm water as well as in short, intermediately long, and long regular head waves. Directly above each individual graph are listed the associated wave length to ship length ratio, λ_w/L , the Froude number, Fr , and the wave height, h_w . A dashed line identifies the force in calm water; a solid fluctuating line, the total longitudinal force in waves; and a dash/dotted line, the mean force in waves. The difference between dashed and dash/dotted lines defines the wave added resistance. This difference is largest in Fig. 12 for all ships, that is, the non-dimensional wave added resistance attains its maximum, as expected, in waves of

length equal to ship length, i.e., when λ_W/L is unity. This is so because at this wave length radiated waves contribute most to the added resistance at this wave length and the relative motion between **hull** and **water surface** is largest.

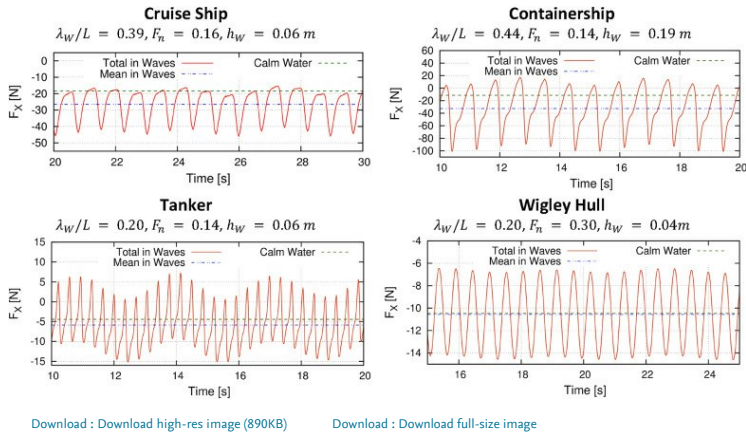


Fig. 11. Computed time histories and mean values of longitudinal force for the investigated ship types (model scale) advancing at constant forward speed in calm water and in short regular head waves.

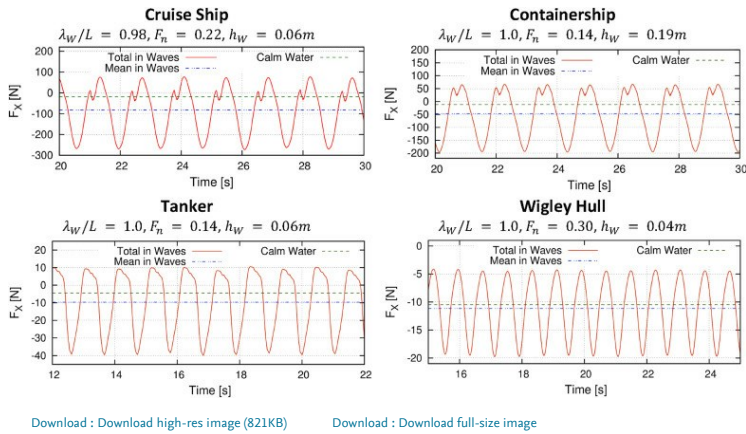


Fig. 12. Computed time histories and mean values of longitudinal force for the investigated ship types (model scale) advancing at constant forward speed in calm water and in intermediately long regular head waves.

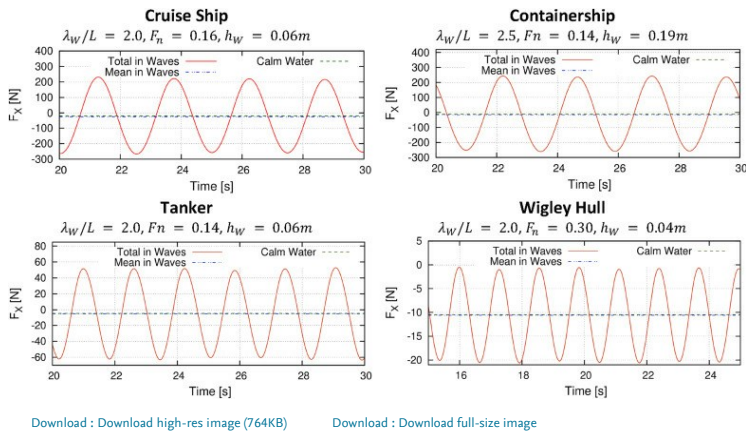


Fig. 13. Computed time histories and mean values of longitudinal force for the investigated ship types (model scale) advancing at constant forward speed in calm water and in long regular head waves.

It is seen that, in short waves, nonlinearities of longitudinal force for the cruise ship and the containership are especially pronounced (see Fig. 11, Fig. 12). It is these ships that are characterized by higher bow flare angles. For the tanker in short waves, low oscillation frequencies are superposed on the encounter frequencies. The mean values were calculated considering these low oscillation frequencies.

6.1. Effects of heave and pitch motions on added resistance in waves

The added resistance in moderate long waves is dominated by radiation. Hence, accurate prediction of motions was required. The comparative response amplitude operators of heave (left) and pitch (right) motions shown in Fig. 14 demonstrate the generally fair agreement between computations and measurements. The maximum value of the response operator is slightly shifted towards longer waves for the blunt ship, i.e., the tanker. Computed heave motions in the range of wave length $\lambda_W/L \approx 0.9$ deviate noticeably from measured motion responses of the cruise ship. We then computed heave and pitch motions using a Rankine source boundary element method (BEM), Söding et al., 2014, Lyu and el Moutar, 2017. BEM and RANS show similar tendency, see Fig. 14 (top). The unexpected deviations between computed and measured heave motions in the range of the above mentioned wave length cannot be explained and might be due to uncertainties related to the measured heave motions.

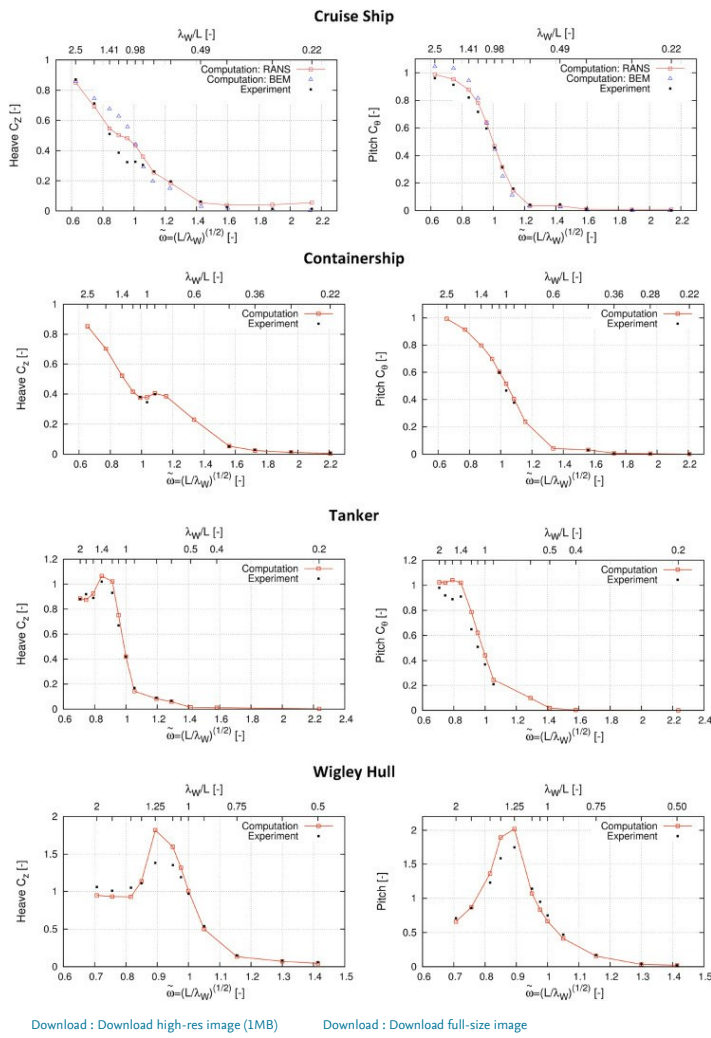
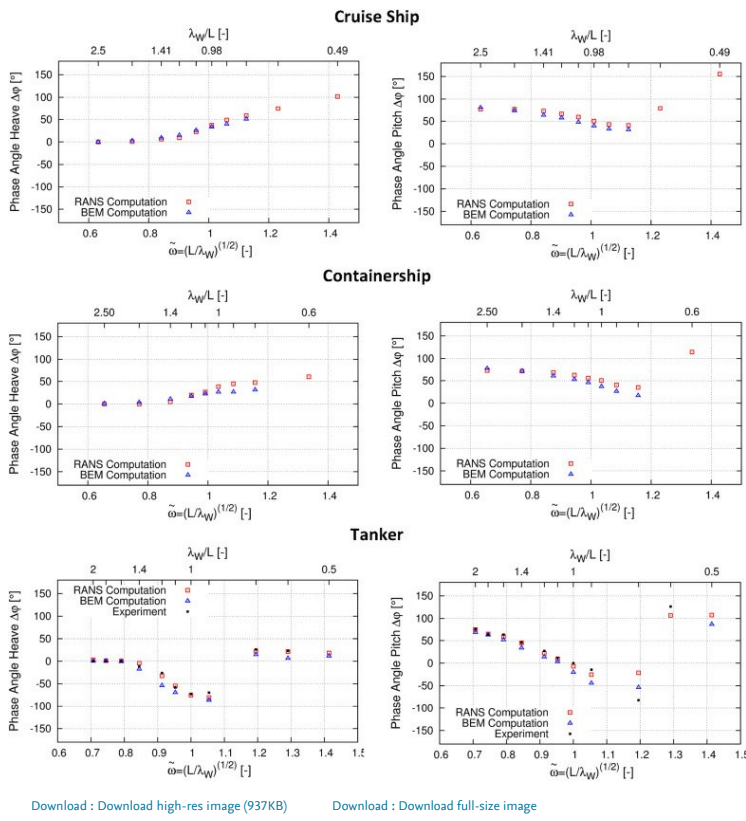


Fig. 14. Computed and measured response amplitude operators of heave (left) and pitch (right) amplitude in regular head waves for the cruise ship at $F_n = 0.22$, the containership at $F_n = 0.14$, the tanker at $F_n = 0.14$, and the Wigley hull at $F_n = 0.30$, [Sigmund and el Moutar \(2017\)](#).

Not only the motion amplitudes, but also their phase angles between incident (head) waves and the particular motions influenced the wave-induced added resistance ([Kashiwagi et al., 2010](#)). [Fig. 15](#) plots these phase angles against wave parameters ω and λ_W/L . For the tanker, experimental measurements were available for comparison; for the containership and the cruise ship, computed results obtained from a boundary element method ([Lyu and el Moutar, 2017](#)) or from RANS simulations. Generally, measurements and computed results correlate favorably. As expected, in short waves the phase angle between wave and heave motion is nearly zero; in long waves ($\lambda_W/L \geq 2$), this phase angle is close to 90deg. In the range of waves where the added resistance attains peak values ($\lambda_W/L \approx 1$), phase angles notably are around 50deg. The only exception is the phase angle of the tanker's heave motion. Here, relative motions between the ship's bow and the wave elevation were largest. This caused pressures acting at the ship's bow to increase, thereby leading to a distinctly higher added resistance. Thus, in the vicinity of peak values of the added resistance, a distinct correlation existed between phase angle and wave-induced added resistance. In short waves ($\lambda_W/L \leq 0.6$), it was impossible to identify clear trends for none of the ships. Although some of these phase angles were large, the associated motion amplitudes were small.

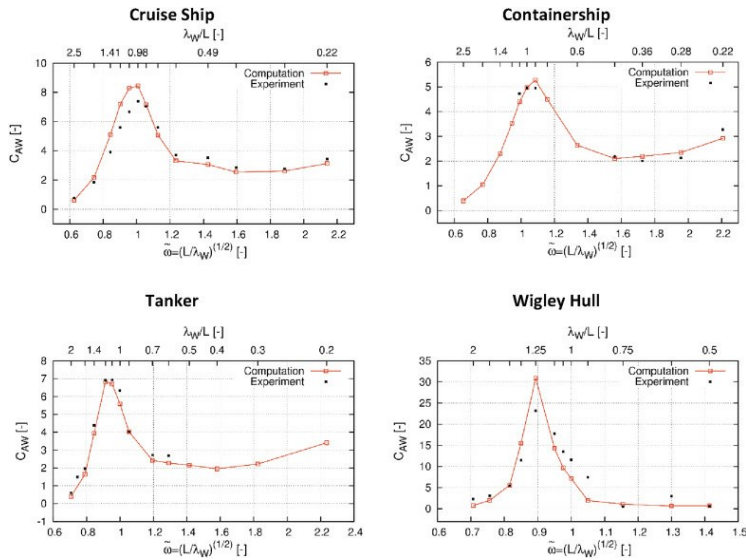


Download : [Download high-res image \(937KB\)](#)

Download : [Download full-size image](#)

Fig. 15. Computed and measured phase angles of heave (left) and pitch (right) motions in regular head waves for the cruise ship at $F_n = 0.16$, the containership at $F_n = 0.14$, and the tanker at $F_n = 0.14$.

The comparable normalized quadratic response amplitude operators of the added resistance in regular head waves, shown in Fig. 16 as plots of the added resistance coefficients, C_{AW} , demonstrate here also the generally favorable agreement between computations and measurements. **Nonlinear effects** in short ($\lambda_W/L < 0.3$) and steep waves are seen to be more pronounced, and often these waves are not harmonic. Computational techniques that account for these (nonlinear) effects are important for an accurate prognosis. Boundary element methods are efficient and offer a good compromise between accuracy and computer time. However, they may be unable to represent entirely these **nonlinear phenomena**. In short waves, the agreement between computations and measurements is especially favorable. Here, **wave diffraction** dominates, and the **wave radiation** part of the added resistance is nearly negligibly small. The increase of the (normalized) added resistance in shorter waves is well predicted by the computations. As mentioned above, the added resistance in short waves is of practical relevance for larger (longer) ships because large ships operate under such conditions most of the time. However, it is appropriate to point out that in very short waves (e.g. $\lambda_W/L \approx 0.2$ and less) the absolute value of the added resistance is relatively small compared to, for example, the calm water resistance. All added resistance coefficients show a significant peak in the range of wave length equal to ship length. Here, ship motions and, consequently, radiation forces are highest. In the range of peak values for the cruise ship, the added resistance coefficient is slightly overestimated. This is due to the relatively larger deviations between computed and measured ship motions (see Fig. 14) at wave frequencies where radiation is dominant.



Download : [Download high-res image \(672KB\)](#)

Download : [Download full-size image](#)

Fig. 16. Computed and measured added resistance coefficients in regular head waves for the cruise ship at $F_n = 0.22$, the containership at $F_n = 0.14$, the tanker at $F_n = 0.14$, and the Wigley Hull at $F_n = 0.30$.

Fig. 17 compares the added resistance coefficients of the four investigated ship types at similar Froude numbers. For the two slender ships (cruise ship and containership), the added resistance in short waves is similar. For the tanker (characterized by a relatively large block coefficient), the added resistance (coefficient) increases in shorter waves, and its peak value shifts towards longer waves.

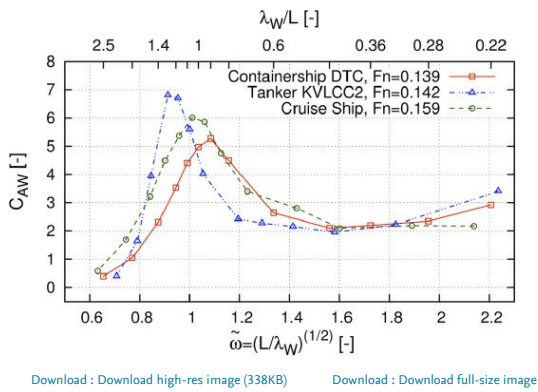


Fig. 17. Comparative computed added resistance coefficients for the cruise ship at $Fr = 0.16$, the containership at $Fr = 0.14$, and the tanker at $Fr = 0.14$.

6.2. Effects of ship speed on added resistance in waves

To investigate effects of ship speed on the wave added resistance, heave and pitch motion and wave added resistance were computed at various forward speeds, albeit only for the cruise ship and the containership. For the cruise ship, computations were performed at full-scale speeds of 15 and 21 kts, corresponding to Froude numbers of 0.16 and 0.22, respectively; for the containership, at 6 and 16 kts, corresponding to Froude number of 0.05 and 0.14, respectively.

The comparative response amplitude operators of heave (left) and pitch (right) motions shown in Fig. 18 demonstrate the generally fair agreement between computations and measurements. It is seen that pitch motions are nearly unaffected by ship speed. In contrast, with heave motions in the range of wave length equal to ship length, this is not the case. In this range of wave lengths, heave motions are distinctly less at slower ship speeds. This is reflected by the associated added resistance coefficients for these two ships presented in Fig. 19. As expected, at slower ship speeds the added resistance in waves is less. This effect is more pronounced at peak values of the added resistance coefficient and in long waves, where radiation is dominant. In short waves, where diffraction is dominant, the effect of ship speed on the added resistance is moderate.

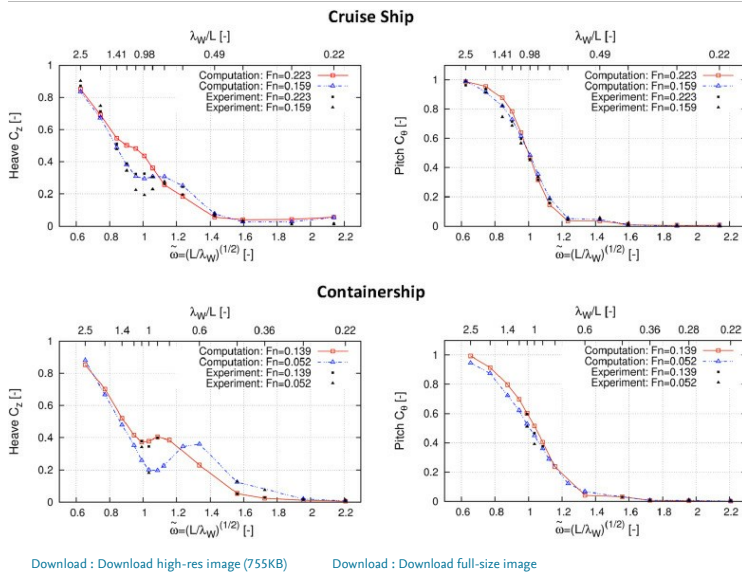


Fig. 18. Response amplitude operators of computed and measured heave (left) and pitch (right) motions for the cruise ship and the containership advancing at two different ship speeds in regular head waves.

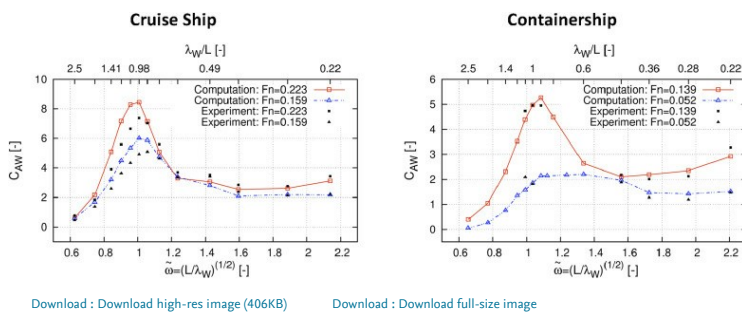


Fig. 19. Comparative computed and measured added resistance coefficients for the cruise ship (left) and the containership (right) advancing at two different ship speeds in regular head waves.

6.3. Effects of viscosity on added resistance in waves

It is assumed that the wave added resistance is driven by pressure forces and hence can be extrapolated using *Froude similarity* (Söding, 1982). Traditional methods such as physical tests and potential theory based methods cannot be used to investigate viscous effects. In the present work the frictional added resistance was determined by subtracting the calm water *friction force* from the mean friction force in waves. Fig. 20 shows computed and measured total added resistance together with the computed frictional component of the added resistance, including its percentage of the total added resistance for all investigated ships. The non-dimensional added *frictional resistance* increases with decreasing *short wave lengths*. It can be seen that especially in short waves, viscous effects on added resistance are significant for all ships. At their peaks, the frictional part contributes about 5% to total the added resistance in waves. In short waves ($\epsilon.g., \lambda_W/L = 0.2$), the frictional part may exceed 20% of the total value.

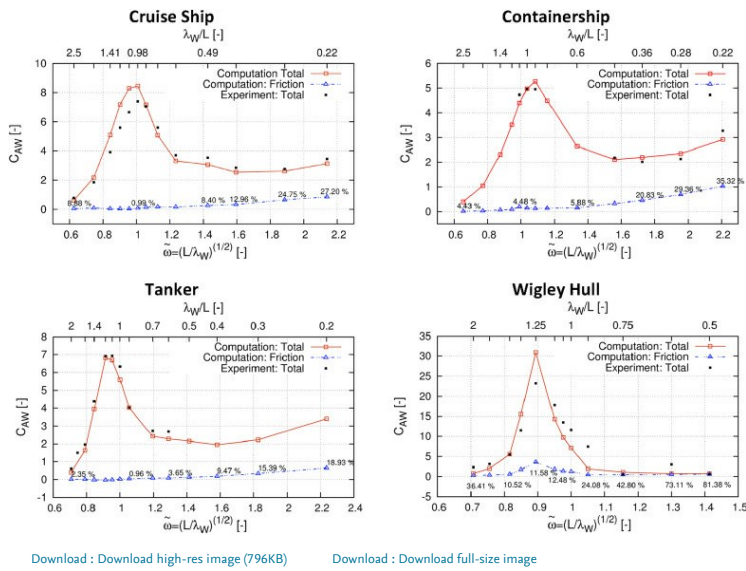


Fig. 20. Computed and measured coefficients of total (red) and frictional (blue) added resistance for the cruise ship at $F_n = 0.22$, the containership at $F_n = 0.14$, the tanker at $F_n = 0.14$ and the Wigley Hull at $F_n = 0.30$ advancing in regular head waves.

To better understand these results, computed representative shear stress distributions on the hulls of the containership and tanker advancing at constant forward speed in calm water and in waves are shown in Fig. 21. The orbital velocities in waves caused the molecular and turbulent shear stresses to increase and led to higher frictional forces acting on the wetted hulls. High shear stresses, marked by dark areas in Fig. 21, are noticeable underneath the wave crests. Beyond that, the viscous pressure distribution in waves may contribute. However, we did not investigate this phenomenon, because it was impossible to readily separate viscous and wave-induced pressures.

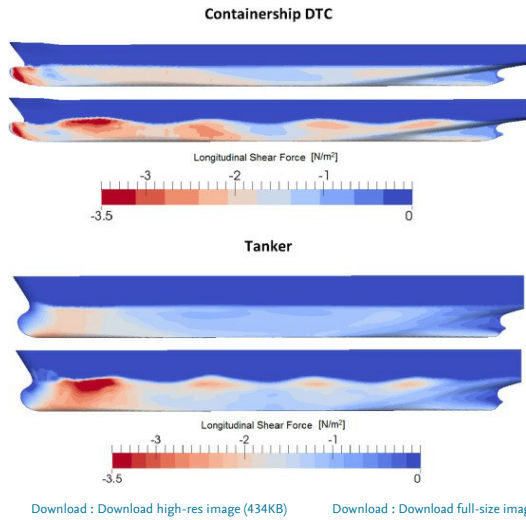


Fig. 21. Representative shear stress distributions of the containership in calm water (upper hull) and in regular head waves (lower hull) for the containership at $F_n = 0.14$ and $Re_c = 6.1 \cdot 10^6$ and the tanker at $F_n = 0.14$ and $Re_c = 2.5 \cdot 10^6$ in model scale.

As mentioned above, all computations so far were performed at model scale. However, viscous effects depend strongly on Reynolds number; therefore, we performed computations in short waves for the cruise ship based on Reynolds numbers corresponding to full-scale conditions and also selected a mean dimensionless wall distance of $y^+ = 1000$ for these computations.

Fig. 22 shows measured and computed coefficients of the total and frictional added resistance at model scale (MS) and full scale (FS) of the containership at $F_n = 0.14$ in regular head waves. As expected, the added frictional resistance is smaller at full scale than at model scale. Its contribution is roughly half that at model scale. Consequently, the frictional component of the added resistance is overestimated when predictions are based on computations at model scale. Nevertheless, this component is still significant and should not be neglected.

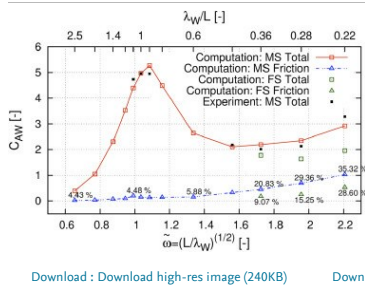


Fig. 22. Computed and measured coefficients of total and frictional added resistance at model scale, $Re_c = 6.1 \cdot 10^6$, and full scale, $Re_c = 2.5 \cdot 10^7$, of the containership at $F_n = 0.14$ in regular head waves.

At this stage let us point out that, in short waves, the total amount of added resistance is relatively small (In some instances, it only amounts to a few percent of calm water resistance for a ship at service speed). That is, in waves the viscous part of the added resistance may not contribute substantially in the total resistance (calm water and added resistance in waves). Nevertheless, these viscous effects may still be useful, e.g., to correct the more efficient potential theory based added resistance predictions.

6.4. Effects of wave steepness on added resistance in waves

Until now, we assumed that the added resistance in waves depends quadratically on wave height (Söding, 1982). However, ships operate in waves of variable steepness. Thus, the question arose in what way this assumption is valid. To resolve this issue, we computed the added resistance in waves for the containership and the tanker in waves of different steepness, here defined as wave height divided by wave length.

For these two ships advancing in head waves of different steepness, Fig. 23 plots our results, together with experimental measurements, in terms of added resistance coefficients plotted against wave length and normalized wave frequency. For the cases investigated, a distinct dependence of added resistance on wave steepness can be observed. At their peaks, added resistance coefficients decrease with increasing wave steepness. In this range of wave lengths radiation is dominant, and nonlinear effects are moderate. In short waves nonlinear effects are important, and diffraction is dominant.

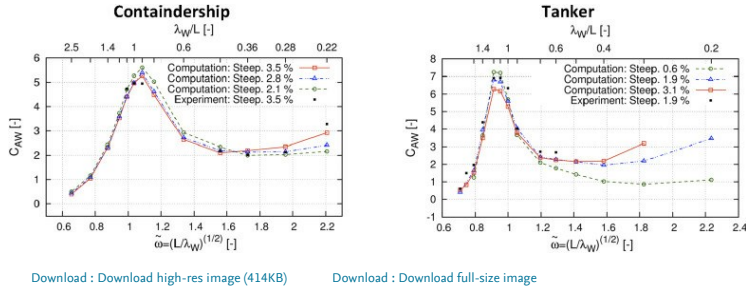


Fig. 23. Computed and measured added resistance coefficients in regular head waves of different steepness for the containership at $F_n = 0.14$ (left) and the tanker at $F_n = 0.14$ (right).

The distinct influence of wave steepness on the added resistance coefficient becomes noticeable in wave lengths that are shorter than one-half ship length ($\lambda_W/L < 0.5$); that is, as waves get shorter, the influence of wave steepness increases. The slope of the added resistance coefficient as wave frequency increases gets distinctly larger with greater wave steepness.

The influence of wave steepness on added resistance is more pronounced for the full-bodied tanker than for the relatively slender containership. In wave lengths of $\lambda_W/L < 0.25$, increasing the wave steepness from 2.1 to 3.5% causes a 35.2% increase of the added resistance coefficient for the containership. In waves of this same length (e.g., when $\lambda_W/L < 0.25$), increasing the wave steepness from 0.6 to 1.9% causes a 201% increase of the added resistance coefficient for the tanker.

An experimental study performed by Yasukawa et al. (2016) shows similar trends. Most of the literature dealing with computational and experimental investigations of added resistance does not specify wave steepness, and one aim of ours was to demonstrate its importance. In this regard, a comparison between computations and experimental measurements of added resistance, especially for ships advancing in short waves, is meaningful only for waves of the same wave steepness.

6.5. Interaction between radiation and diffraction forces

Often, potential flow methods separate wave-induced forces into radiation and diffraction. This simplifies the solution and is expedient for linear problems. Regarding added resistance in waves, here we investigated the interaction between radiation and diffraction.

To quantify these interactions, we determined diffraction and radiation forces separately for the four investigated ship types. To this end, we performed three different computations. First, we computed total added resistance in waves. Second, we determined added resistance of the fixed ships advancing with constant forward speed in incoming head waves (diffraction). Third, we obtained added resistance of the moving ships advancing in calm water by prescribing the computed motions obtained in the first step (radiation).

Fig. 24 plots computed and measured total resistance as well as the associated computed radiation and diffraction forces against wave length to ship length ratios as well as against normalized wave frequencies. Although interaction between radiation and diffraction is more pronounced in long waves, it vanished almost completely in short waves, as was expected. In long waves (e.g., when $\lambda_W/L > 1$) the radiation part of added resistance becomes significant, and the diffraction part is only moderately influenced by waves. Nevertheless, interaction between radiation and diffraction was important. In short waves (e.g., when $\lambda_W/L < 0.50$) radiation forces are nearly zero, and diffraction forces depend only moderately on wave frequency. Thus, in short waves diffraction forces match total added resistance. Consequently, the radiation part of the added resistance coefficients display a significant peak in the range of large motion response (e.g., when $\lambda_W = L$). These findings were found to be valid for all ships at all Froude numbers. The interaction between radiation and diffraction was addressed and discussed by Kashiwagi et al. (2010).

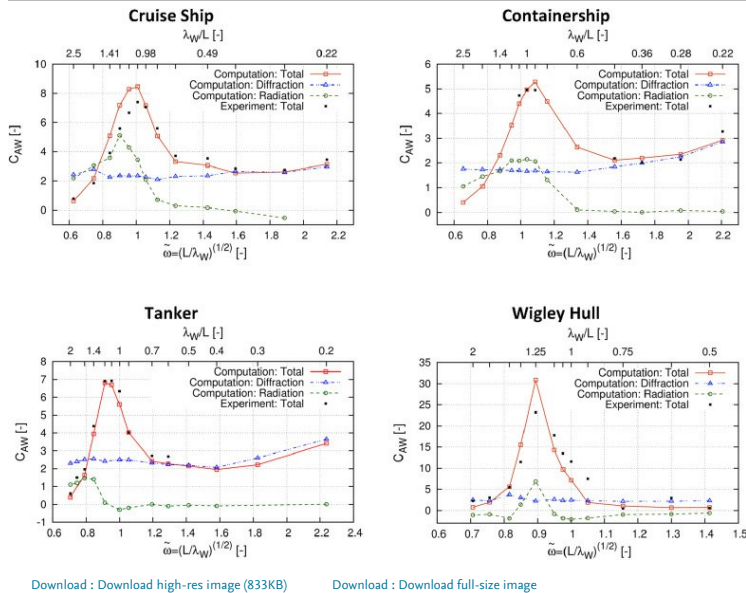


Fig. 24. Added resistance coefficients of total added resistance (solid), diffraction force (dotted line), and radiation force (dashed line) for the cruise ship at $F_n = 0.22$, the containership at $F_n = 0.16$, the tanker at $F_n = 0.14$, and the Wigley hull at $F_n = 0.3$.

7. Conclusions

Predicting wave added resistance of ships remains challenging. Nevertheless, the practical relevance of this subject motivated systematic investigations in the use of advanced numerical methods to analyze added resistance of ships in waves.

Initially, we investigated discretization errors. Then, based on the outcome, we identified spatial and time dependent discretizations suitable for simulations. Furthermore, we introduced appropriate numerical methods to predict the added resistance in waves. Two findings were important. On the one hand, computations of calm water resistance as well as added resistance in waves should be carried out on the same numerical grid. On the other hand, the added resistance should be normalized always against the actual wave amplitude, not the targeted wave amplitude.

Ship motions and the added resistance in waves were computed for the four ship types and compared to experimental model test measurements. Generally, computations and measurements correlated favorably. This was also so for added resistances in short and long waves, thereby demonstrating that the methods based on solving the Reynolds-averaged Navier-Stokes equations were capable of predicting reliable wave-induced first- and higher-order responses, such as ship motions and added resistance in waves, respectively.

Results showed that radiation forces were affected more strongly by ship speed than diffraction forces. Thus, peaks of added resistance coefficients were less pronounced at lower ship speeds.

By subtracting **frictional resistance** in calm water from frictional resistance in waves, the frictional added resistance was determined. Computations showed that, in short waves, friction accounted for a significant part of the total added resistance, namely, of 20% or even more. However, full scale computations showed that this effect was less pronounced at full-scale.

Diffraction and radiation forces at different frequencies were investigated, whereby diffraction forces were obtained by restraining the ship in waves and the radiation forces, by prescribing the motions of the ship in calm water. In long waves, the sum of diffraction and radiation forces did not match the total resistance, i.e., the interaction of these two force components had to be accounted for. In short waves, the diffraction part of total resistance was dominant as almost no ship motions were induced.

Generally, the assumption of a quadratic correlation between wave height and added resistance was confirmed for ships advancing in waves of moderate to long wave lengths. However, this assumption did not hold for ships advancing in short waves, because in short **waves diffraction** was dominant.

Acknowledgments

The research was supported by the German Federal Ministry of Economic Affairs under contract [03Sx339B](#) and Energy and by the European Union under contract [FP7-SST-2013-RTD-1](#). The authors thank Jens Ley for helping to set up the computations for the cruise vessel.

[Recommended articles](#) [Citing articles \(25\)](#)

References

Boese, 1970 P. Boese

A simple method for the calculation of resistance increase of a ship in a seaway

J. Ship Technol. Res., 17 (86) (1970)

[Google Scholar](#)

Brunswig and el Moctar, 2004 J. Brunswig, O. el Moctar

Prediction of ship motions in waves using RANSE

Proc. Of the 7th Numerical Towing Tank Symposium (NUTTS), Hamburg, Germany (2004)

[Google Scholar](#)

Carrica et al., 2011 P.M. Carrica, H. Fu, F. Stern

Computations of self-propulsion free to sink and trim and of motions in head waves of the KRISO Container Ship (KCS) model

Appl. Ocean Res., 33 (2011) (2011), pp. 309-320

[Article](#)  [Download PDF](#) [View Record in Scopus](#) [Google Scholar](#)

CD ADAPCO, 2011 CD ADAPCO

User Guide 6.02.007

(2011)

[Google Scholar](#)

Duan and Li, 2013 W. Duan, C. Li

Estimation of added resistance for large blunt ship in waves

J. Mar. Sci. Appl., 12 (1) (2013), pp. 1-12

[CrossRef](#) [View Record in Scopus](#) [Google Scholar](#)

el Moctar et al., 2010 B. el Moctar, V. Shigunov, T. Zorn

Duisburg test case: post- panamax container ship for benchmarking

Ship Technol. Res. J., 59/3 (2010), pp. 50-64

[Google Scholar](#)

el Moctar, 2001 O. el Moctar

Numerical computations of flow forces in ship manoeuvring

Ship Technol. Res. (2001), pp. 98-123

[View Record in Scopus](#) [Google Scholar](#)

el Moctar et al., 2017 O. el Moctar, J. Ley, J. Oberhagemann, T.E. Schellin

Advanced computational methods for hydroelastic effects of ships in extreme seas

Ocean. Eng., 130 (2017), pp. 659-673

[Article](#)  [Download PDF](#) [View Record in Scopus](#) [Google Scholar](#)

el Moctar et al., 2011 O. el Moctar, J. Oberhagemann, T. Schellin

Free surface RANS method for hull girder springing and whipping

SNAME Trans., 119 (2011), pp. 48-66

[View Record in Scopus](#) [Google Scholar](#)

el Moctar et al., 2016a O. el Moctar, S. Sigmund, J. Ley, T.E. Schellin

Numerical and experimental analysis of added resistance of ships in waves

J. Offshore Mech. Arct. Eng., 139 (1) (2016), Article 011301

[Google Scholar](#)

el Moctar et al., 2016b O. el Moctar, F. Sprenger, T. Schellin, A. Papanikolaou

Numerical and experimental investigations of ship maneuvers in waves

Proceedings of the 35th International Conference on Ocean, Offshore & Arctic Engineering OMAE, vol. 2016 (2016)

Busan, South Korea

[Google Scholar](#)

Faltinsen et al., 1980 O.M. Faltinsen, K. Minsaas, N. Liapis, S.O. Skjördal

Prediction of resistance and propulsion of a ship in a seaway

The 13th Symposium on Naval Hydrodynamics (1980), pp. 505-529

[View Record in Scopus](#) [Google Scholar](#)

Ferziger and Peric, 2002 J. Ferziger, M. Peric

Computational Methods for Fluid Dynamics

(third ed.), Berlin Heidelberg New York: Springer, Berlin (2002)

[Google Scholar](#)

Gerritsma and Beukelman, 1972 J. Gerritsma, W. Beukelman

Analysis of the resistance increase in waves of a fast cargo ship

Int. Shipbuild. Prog., 19 (1972), pp. 285-293

[CrossRef](#) [View Record in Scopus](#) [Google Scholar](#)

Guo and Steen, 2011 B. Guo, S. Steen

Evaluation of added resistance of kvcc2 in short waves

J. Hydrodyn., 23 (6) (2011), pp. 709-722

[Article](#)  [Download PDF](#) [CrossRef](#) [View Record in Scopus](#) [Google Scholar](#)

Hadler, 1958 J. Hadler

Coefficients for International Towing Tank Conference 1957 Model Ship Correlation Line


DTIC Document (1958)
Tech. rep.
[Google Scholar](#)

[International Towing Tank Conference, 2008](#) International Towing Tank Conference
Testing and Data Analysis - Resistance Test
(2008)
Procedure 7.5-02-02-01
[Google Scholar](#)

[Joosen, 1966](#) W.P. Joosen
Added resistance in waves
6th Symposium on Naval Hydrodynamics (1966)
[Google Scholar](#)

[Journée, 2003](#) J. Journée
Experiments and Calculations on 4 Wigley Hull Forms in Head Waves. Netherlands 1992
Delft University of Technology, Ship Hydromechanics Laboratory (2003)
Neudruck des Berichts 0909(1992)
[Google Scholar](#)

[Kashiwagi et al., 2010](#) M. Kashiwagi, T. Ikeda, T. Sasakawa
Effects of forward speed of a ship on added resistance in waves
J. Offshore Polar Eng., 20 (3) (2010), pp. 196-203
[View Record in Scopus](#) [Google Scholar](#)


[Kim and Kim, 2011](#) K. Kim, Y. Kim
Numerical study on added resistance of ships by using a time-domain Rankine panel method
Ocean. Eng., 38 (13) (2011), pp. 1357-1367
[Article](#)  [Download PDF](#) [View Record in Scopus](#) [Google Scholar](#)

[Kim et al., 2012](#) K.-H. Kim, M.-G. Seo, Y. Kim
Numerical analysis on added resistance of ships
Int. J. Offshore Polar Eng., 22 (1) (2012), pp. 21-29
[View Record in Scopus](#) [Google Scholar](#)

[Kuroda et al., 2008](#) M. Kuroda, M. Tsujimoto, T. Fujiwara, S. Ohmatsu, K. Takagi
Investigation on components of added resistance in short waves
J. Jpn. Soc. Nav. Archit. Ocean Eng., 8 (2008), pp. 171-176
[CrossRef](#) [View Record in Scopus](#) [Google Scholar](#)

[Larsson et al., 2010](#) L. Larsson, F. Stern, M. Visonneau
A Workshop on Numerical Ship Hydrodynamics
Proceedings, vol. II (2010)
(Göteborg)
[Google Scholar](#)

[Ley et al., 2014](#) J. Ley, S. Sigmund, B. el Moctar
Numerical prediction of the added resistance of ships in waves
Proceedings of the ASME 33th International Conference on Ocean, Offshore and Arctic Engineering (2014)
San Francisco: OMAE 2014
[Google Scholar](#)

[Liu et al., 2011](#) S. Liu, A. Papanikolaou, G. Zaraphonites
Prediction of added resistance of ships in waves
J. Ocean. Eng., 38 (2011), pp. 641-650
[Article](#)  [Download PDF](#) [View Record in Scopus](#) [Google Scholar](#)

[Lyu and el Moctar, 2017](#) W. Lyu, O. el Moctar
Numerical and experimental investigations of wave-induced second order hydrodynamic loads
Ocean. Eng. (2017), pp. 197-212
[Article](#)  [Download PDF](#) [View Record in Scopus](#) [Google Scholar](#)

[Maruo, 1957](#) H. Maruo
The excess resistance of a ship in a rough sea
Int. Shipbuild. Prog., 4 (1957), pp. 337-345
[CrossRef](#) [View Record in Scopus](#) [Google Scholar](#)

[Maruo, 1960](#) H. Maruo
The drift force on a body floating in waves
J. Ship Res. (1960), pp. 1-10
[View Record in Scopus](#) [Google Scholar](#)

[Maruo, 1963](#) H. Maruo
Resistance in waves
Society Nav. Archit. Jpn., 8 (1963)
60th anniversary Series
[Google Scholar](#)

[Menter, 1994](#) F.R. Menter
Two-equation eddy-viscosity turbulence models for engineering applications
AIAA J., 32 (8) (1994), pp. 1598-1605
[CrossRef](#) [View Record in Scopus](#) [Google Scholar](#)

[Muzaferija and Peric, 1999](#) S. Muzaferija, M. Peric
Computation of Free-surface Flows Using Interface-tracking and Interface-capturing Methods
Computational mechanics publications (1999)
[Google Scholar](#)

[Nietzschmann, 2010](#) T. Nietzschmann
Widerstands- und Propulsionsversuch für das Modell eines Containerschiffes
SVA Potsdam Model Basin report (2010)
[Google Scholar](#)

[Oberhagemann and el Moctar, 2007](#) J. Oberhagemann, O. el Moctar
A simplified approach to investigate fluid-structure coupling effects on slamming loads of ships
Proc. 10th Numerical Towing Tank Symposium (2007), pp. 150-155
(Hamburg)
[View Record in Scopus](#) [Google Scholar](#)

Oberhagemann et al., 2012 J. Oberhagemann, V. Shigunov, O. el Mactar

Application of CFD in long-term extreme value analyses of wave loads

Ship Technol. Res., 59 (3) (2012), pp. 4-22

[CrossRef](#) [View Record in Scopus](#) [Google Scholar](#)

OpenFOAM, 2011-2016 OpenFOAM

User Guide. OpenFOAM Foundation

(2011-2016)

[Google Scholar](#)

OpenFOAM, 2016 OpenFOAM

Openfoamwiki. Retrieved from OpenFOAM Guide/The PIMPLE Algorithm in OpenFOAM

(2016)

https://openfoamwiki.net/index.php/OpenFOAM_guide/The_PIMPLE_algorithm_in_OpenFOAM

[Google Scholar](#)

Sadat-Hosseini et al., 2013 H. Sadat-Hosseini, P.-C. Wu, P.M. Carrica, H. Kim, Y. Toda, F. Stern

CFD verification ad validation of added resistance and motions of KVLCC2 with fixed and free surge in short and long head waves

Ocean. Eng., 59 (2013), pp. 240-273

[Article](#) [Download PDF](#) [View Record in Scopus](#) [Google Scholar](#)

Salvesen, 1978 N. Salvesen

Added resistance of ships in waves

J. Hydrodyn., 12 (1) (1978), pp. 24-34

[CrossRef](#) [View Record in Scopus](#) [Google Scholar](#)

Salvesen et al., 1970 N. Salvesen, O. Tuck, O. Faltinsen

Ship motions and sea loads

SNAME Trans., 78 (1970), pp. 250-287

[Google Scholar](#)

Schellin and el Mactar, 2007 T. Schellin, O. el Mactar

Numerical prediction of impact-related wave loads on ships

ASME J. Offshore Mech. Arct. Engg., 129 (1) (2007), pp. 39-47

[CrossRef](#) [View Record in Scopus](#) [Google Scholar](#)

Seo et al., 2013 M. Seo, D. Park, K. Yang, Y. Kim

Comparative study on computation of ship added resistance in waves

Ocean. Eng., 73 (C) (2013), pp. 1-15

[Article](#) [Download PDF](#) [View Record in Scopus](#) [Google Scholar](#)

Seo et al., 2014 M. Seo, K. Yang, D. Park, Y. Kim

Numerical analysis of added resistance on ships in short waves

Ocean. Eng., 73 (C) (2014), pp. 1-15

[View Record in Scopus](#) [Google Scholar](#)

Sigmund and el Mactar, 2017 S. Sigmund, O. el Mactar

Numerical and experimental investigation of propulsion in waves

Ocean. Eng., 144 (2017), pp. 35-49

[Article](#) [Download PDF](#) [View Record in Scopus](#) [Google Scholar](#)

Simman, 2008 Simman

Retrieved from

<http://www.simman2008.dk/KVLCC/KVLCC2/tanker2.html> (2008)

Simonsen et al., 2013 C.D. Simonsen, J.F. Otzen, S. Jonquez, F. Stern

EFD and CFD for KCS heaving and pitching in regular head wave

J. Mar. Sci. Technol., 18 (4) (2013), pp. 435-459

[CrossRef](#) [View Record in Scopus](#) [Google Scholar](#)

Söding, 1982 H. Söding

Bewegungen und Belastungen der Schiffe im Seegang. Vorlesungsmanuskript Nr. 18

Institut Für Schiffbau Der Universität Hamburg (1982)

[Google Scholar](#)

Söding et al., 2014 H. Söding, V. Shigunov, T. Schellin, O. el Mactar

A rankine panel method for added resistance of ships in waves

ASME J. Offshore Mech. Arct. Eng., 136 (2014)

[Google Scholar](#)

Söding et al., 2012 H. Söding, A. von Graefe, V. Shigunov, O. el Mactar

Rankine source method for seakeeping predictions

Proc. 31th Int. Conf. On Ocean, Offshore and Arctic Eng. OMAE (2012), pp. 2012-83450

[Google Scholar](#)

About ScienceDirect

Remote access

Shopping cart

Advertise

Contact and support

Terms and conditions

Privacy policy

Sprenger et al., 2016 F. Sprenger, A. Maron, G. Delefortrie, A. Papanikolaou

We use cookies to help enhance our service and tailor content and ads. By continuing you agree to the use of cookies.

Experimental studies on seakeeping and manoeuvrability in adverse weather conditions

Proceedings SNAME2016 Annual Conference (2016)

(Seattle)

[Google Scholar](#)

Ström-Tejsen et al., 1973 H.J. Ström-Tejsen, Y. Yeh, D. Moran

Added resistance in waves

SNAME Trans., 81 (1973), pp. 109-143

[View Record in Scopus](#) [Google Scholar](#)

Turnock et al., 2014 S. Turnock, H. Tanaka, J. Kim, B. Wu, T. Fu, A. Takinaci, T. Mikkola

The resistance committee-final report and recommendations to the 27th ITTC

Proceeding of 27th International Towing Tank Conference (2014)

[Google Scholar](#)

Valanto and Hong, 2015 P. Valanto, Y. Hong

Experimental Investigation of Ship Waves Addes Resistance in Regular Head, Oblique, Beam and Following Waves

(2015)

Hawai, USA: ISOPE 2015



About ScienceDirect

Remote access

Shopping cart

Advertise

Contact and support

Terms and conditions

Privacy policy

Sprenger et al., 2016 F. Sprenger, A. Maron, G. Delefortrie, A. Papanikolaou

We use cookies to help enhance our service and tailor content and ads. By continuing you agree to the use of cookies.

Experimental studies on seakeeping and manoeuvrability in adverse weather conditions

Proceedings SNAME2016 Annual Conference (2016)

(Seattle)

[Google Scholar](#)

Ström-Tejsen et al., 1973 H.J. Ström-Tejsen, Y. Yeh, D. Moran

Added resistance in waves

SNAME Trans., 81 (1973), pp. 109-143

[View Record in Scopus](#) [Google Scholar](#)

Turnock et al., 2014 S. Turnock, H. Tanaka, J. Kim, B. Wu, T. Fu, A. Takinaci, T. Mikkola

The resistance committee-final report and recommendations to the 27th ITTC

Proceeding of 27th International Towing Tank Conference (2014)

[Google Scholar](#)

Valanto and Hong, 2015 P. Valanto, Y. Hong

Experimental Investigation of Ship Waves Addes Resistance in Regular Head, Oblique, Beam and Following Waves

(2015)

Hawai, USA: ISOPE 2015

RELX™

FEEDBACK

[Google Scholar](#)

Yasukawa et al., 2016 H. Yasukawa, A. Matsumoto, S. Ikezoe

Wave height effect on added resistance of full hull ships in waves

Jpn. Soc. Nav. Architects Ocean Eng. JASNAOE (2016), pp. 45-54

[CrossRef](#) [View Record in Scopus](#) [Google Scholar](#)

[View Abstract](#)

© 2017 Elsevier Ltd. All rights reserved.

FEEDBACK 